Abaqus implementation of monolithic and staggered schemes for quasi-static and dynamic fracture phase-field model

Guowei Liu [a], Qingbin Li [a,*], Mohammed A. Msekh [b], Zheng Zuo [a,c]

[a] State Key Laboratory of Hydroscience and Engineering, Tsinghua University, Beijing 100084, China
[b] Civil Engineering Department, College of Engineering, University of Babylon, Babylon, Iraq
[c] China Power Complete Equipment Co., Ltd., Beijing 100080, China

ABSTRACT

The phase-field model for fractures regularizes crack diffusion using a length-scale parameter. The displacement fields and the phase-field in a coupled system can be solved as either fully coupled "monolithic" or sequentially coupled "staggered" fields. In this paper, we employ the commercial finite-element software Abaqus to solve the monolithic and staggered phase-field models using a user-defined element (UEL) and user-defined material (UMAT/VUMAT) subroutines in two- and three-dimensions for quasi-static and dynamic fractures. We present the implementation procedures for both strategies, and make a detailed comparison using different applications. By comparing the phase-field model as a diffusive crack model and the extended finite-element method (XFEM) as a discrete crack model, we obtain good agreement. We investigate the influence of the model-regularization parameter based on experimental results. We adopt the thread-parallel execution and mutexes of Abaqus solvers.

© 2016 Elsevier B.V. All rights reserved.

1. Introduction

Crack propagation in solids is an important research topic in the field of engineering. Hence, different numerical approaches and models have been studied. In recent years, various methods have been introduced, such as discrete crack models, the extended finite-element method (XFEM) [1–5], generalized finite-elements method (GFEM) [6], and the phantom-node method [7], but they are all based on the division of the unity method in which the displacement field is enriched with discontinuities. Another common method employed to separate the fracture surfaces is the element-erosion technique [8–11], where the stresses are set to zero in the elements satisfying the failure criterion. Element-erosion methods cannot simulate crack branching correctly [12]. Crack branching was first simulated by the inter-element crack method [13,14], where a crack is modeled by dividing the elements' edges. In addition to modifying the constitutive model, diffusive crack models [15,16] do not explicitly track macroscopic crack paths, and they ensure the dissipation of an accurate quantity of energy.

Presently, the variational theory in fractures represented by phase-field techniques for fracture mechanics has attracted significant interest. The phase-field model expresses the cracks by utilizing a scalar field that is determined by two partial differential equations. Because no ad hoc works are required to track crack geometry, phase-field approaches have a distinct advantage in the detection of crack bifurcation and crack propagation in three-dimensional (3D) continua compared with discrete fracture models. In terms of their mathematical formulation, phase-field models can be formulated based on Landau models in physics [17,18] or the variational approach to fracture in mechanics [19–21]. The latter is an extension of the classical Griffith fracture theory. In terms of implementation algorithms, phase-field models can be solved in either a monolithic scheme [21–24] or staggered scheme [25–27]. In other words, the displacement field and the phase field can be solved simultaneously or separately. Borden et al. [26] incorporated the phase-field model into the isogeometric analysis so that the high-order phase-field model [28] can be carried out. Furthermore, phase-field formulations have been developed to deal with cohesive fractures [29], large strain problems [30], multiphysics [31], and in ductile fracture [32,33].

The commercial software Abaqus is widely used in research and industry, and it has incorporated the smeared crack-concrete model, the element-erosion method, the cohesive models and the XFEM [34,35]. In addition to using the flexibility and capability to track complex cracks using phase-field methods, Abaqus is efficient when used for nonlinear analyses. Msekh et al. [24] implemented a fully coupled phase-field model in Abaqus using a user-defined element (UEL) subroutine to model quasi-static mode-I fractures.

* Corresponding author.
  E-mail address: qingbinli@mail.tsinghua.edu.cn (Q. Li).

In this work, the phase-field model presented by Miehe et al. [20,21] is implemented in Abaqus in both solution schemes. The elastic strain energy density is decomposed to distinguish between fractures in compression and tension; therefore, mode-II fractures and dynamic fractures are solved. The staggered scheme is implemented using user-defined material (UMAT/VUMAT) subroutines. This implementation enables Abaqus to solve the nonlinear equations of motion implicitly and explicitly. We also solve quasi-static and dynamic fracture benchmarks in order to compare the phase-field model and XFEM method. We adopted the parallel solvers of Abaqus in order to overcome the computational cost of the phase-field model. We also studied the number of CPUs that affects the time needed to run the phase-field model.

The paper is structured as follows. In Section 2, we present the basic equations of the phase-field model based on the variational approach to brittle fractures. In Section 3, we present the computational implementation of the fully coupled and sequentially coupled phase-field models in Abaqus. In Section 4, we investigate several numerical examples including two-dimensional (2D) and 3D cases under quasi-static and dynamic loading, respectively. In Section 5, we discuss the parallel computing implementation of the models, and in Section 6, we summarize the paper.

2. Formulation

2.1. Phase-field approximation

Denoting a linear elastic body $\Omega \subset R^d (d \in \{1,2,3\})$, surface boundary $\partial\Omega$, and internal crack surface as Γ, the crack surface can be represented using both the internal displacement discontinuity and the regularized crack surface function of the phase-field $\phi(\mathbf{x},t)$ variable (see Fig. 1).

In the fracture modeling of brittle materials, the total potential energy of the body (Π) is the sum of the deformation energy and the crack surface energy:

$$\Pi(\mathbf{u},\Gamma) = \int_\Omega \psi_e(\boldsymbol{\varepsilon}(\mathbf{u}))\mathrm{d}V + \int_\Gamma G_c\mathrm{d}\Gamma \tag{1}$$

where ψ_e is the elastic strain-energy density function, $\mathbf{u} \in R^d$ is the displacement, and G_c is the critical energy release rate. Considering the small-strain theory, the linearized strain tensor can be defined in terms of the displacement gradient:

$$\boldsymbol{\varepsilon} = \frac{1}{2}\left(\nabla\mathbf{u} + \nabla^T\mathbf{u}\right) \tag{2}$$

Francfort and Marigo [19] proposed the idea that cracks should propagate along a path of the least energy and satisfy the irreversibility: $\Gamma(s) \subseteq \Gamma(t)$ for all $s < t$. The variational approach to

fractures is the inheritance and development of the classical Griffith theory. This approach compensates for the inadequacy of classical fracture mechanics in terms of predicting crack initiation and bifurcation.

The numerical implementation of the variational approach was proposed by Bourdin et al. [20] and developed by Miehe et al. [21], who introduced an auxiliary phase-field variable to express cracks. Therefore, the crack surface energy can be approximated by:

$$\int_\Gamma G_c\mathrm{d}\Gamma \approx \int_\Gamma G_c\left[\frac{\phi^2}{2l_0} + \frac{l_0}{2}|\nabla\phi|^2\right]\mathrm{d}V \tag{3}$$

where the regularization parameter l_0 controls the width of the smooth approximation of the crack.

In order to maintain the compressive resistance during crack closure, the strain tensor is decomposed into positive and negative quantities as follows:

$$\boldsymbol{\varepsilon} = \boldsymbol{\varepsilon}^+ + \boldsymbol{\varepsilon}^- \tag{4}$$

and

$$\boldsymbol{\varepsilon}^\pm = \sum_{a=1}^d \langle\varepsilon_a\rangle^\pm \mathbf{n}_a \otimes \mathbf{n}_a \tag{5}$$

where $\boldsymbol{\varepsilon}^+$ and $\boldsymbol{\varepsilon}^-$ represent the tensile and compressive modes of $\boldsymbol{\varepsilon}$, respectively. ε_a and $\mathbf{n}_a$ are the eigenvalues and eigenvectors of $\boldsymbol{\varepsilon}$ in d dimensions. The Macaulay brackets are defined as: $\langle x\rangle_\pm = (x \pm |x|)$. Hence, the elastic energy can be decomposed into a positive part and a negative part [21]:

$$\int_\Omega \psi_e(\boldsymbol{\varepsilon})\mathrm{d}V = \int_\Gamma \left(\left[(1-\phi)^2 + \kappa\right]\psi_e^+(\boldsymbol{\varepsilon}) + \psi_e^-(\boldsymbol{\varepsilon})\right)\mathrm{d}V \tag{6}$$

and

$$\psi_e^\pm(\boldsymbol{\varepsilon}) = \frac{\lambda}{2}\langle\mathrm{tr}(\boldsymbol{\varepsilon})\rangle^2 + \mu\mathrm{tr}\left[\left(\boldsymbol{\varepsilon}^\pm\right)^2\right] \tag{7}$$

where ψ_e^+ and ψ_e^- represent the tensile and compressive modes in ψ_e, respectively. The model parameter $\kappa \ll 1$ prevents numerical singularity in the case of partly or fully broken systems.

2.2. Governing equations

In the dynamic case, the kinetic energy of the body is given by:

$$T(\dot{\mathbf{u}}) = \int_\Omega \frac{1}{2}\rho\dot{\mathbf{u}}\cdot\dot{\mathbf{u}}\mathrm{d}V \tag{8}$$

where ρ is the mass density of the material and $\dot{\mathbf{u}}$ denotes the local velocity. By adding the kinetic energy to the energy-storage func-
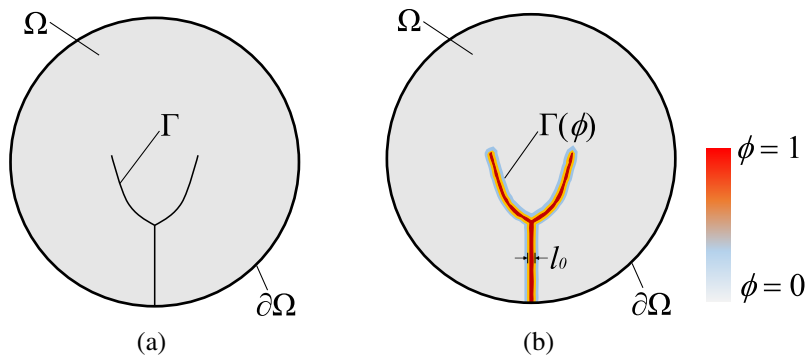

Fig. 1. Body with an internal crack: (a) sharp crack; (b) diffusive crack.

tional (6) and the dissipation function (3), the Lagrangian can be expressed as:

$$L = T - \Pi = \int_\Omega \frac{1}{2}\rho\dot{\boldsymbol{u}}\cdot\dot{\boldsymbol{u}}\mathrm{d}V - \int_\Omega\left\{\left[(1-\phi)^2+\kappa\right]\psi_e^+(\boldsymbol{\varepsilon})+\psi_e^-(\boldsymbol{\varepsilon})\right\}\mathrm{d}V$$
$$- \int_\Omega G_c\left[\frac{\phi^2}{2l_0}+\frac{l_0}{2}|\nabla\phi|^2\right]\mathrm{d}V \tag{9}$$

According to Hamilton's principle, the variation of L with respect to the two fields $\{\boldsymbol{u},\phi\}$, considering $\delta\boldsymbol{u}=0$ on $\partial\Omega$, yields the Euler–Lagrange equations:

$$\begin{cases} \mathrm{Div}[\boldsymbol{\sigma}] = \rho\ddot{\boldsymbol{u}} \\ \left(\frac{G_c}{l_0}+2\psi_e^+\right)\phi - G_cl_0\Delta\phi = 2\psi_e^+ \end{cases} \tag{10}$$

in the domain Ω along with the boundary conditions:

$$\begin{cases} \boldsymbol{\sigma}\cdot\boldsymbol{n}^* = \boldsymbol{t}^* & \text{on } \partial\Omega_{t^*} \\ \nabla\phi\cdot\boldsymbol{n}^* = 0 & \text{on } \partial\Omega \end{cases} \tag{11}$$

where $\boldsymbol{t}^*$ is a prescribed traction force on $\partial\Omega$ and $\boldsymbol{n}^*$ is the outward-pointing normal vector of the boundary. The first equation in (10) is the equilibrium equation, and the second one is the phase-field evolution equation. The stress tensor can be obtained from the strain derivative of the elastic energy:

$$\boldsymbol{\sigma} = \partial_\varepsilon\psi_e$$
$$= \left[(1-\phi)^2+\kappa\right]\left(\lambda\langle\mathrm{tr}(\boldsymbol{\varepsilon})\rangle_+\mathbf{1}+2\mu\boldsymbol{\varepsilon}_+\right)$$
$$+ \left(\lambda\langle\mathrm{tr}(\boldsymbol{\varepsilon})\rangle_-\mathbf{1}+2\mu\boldsymbol{\varepsilon}_-\right) \tag{12}$$

In order to prevent cracks from healing when ψ_e^+ decreases, we adopted the local history field of the maximum positive reference energy [25]:

$$\mathcal{H}(\boldsymbol{x},t) = \max_{s\in[0,t]}\psi_e^+(\boldsymbol{\varepsilon}(\boldsymbol{x},s)) \tag{13}$$

which replaces ψ_e^+ in the expression (10) so that the inequality constraint is enforced locally.

In the formulation (10), the phase-field model can have homogeneous solutions by ignoring the spatial derivatives of ϕ [36–38]. Fig. 2 shows the characteristic plots of the homogenous stress and phase field versus the homogenous strain. We observed that when l_0 decreases, the maximum tensile stress increases. In fact, the maximum tensile stress and corresponding critical strain can be written as:

$$\sigma_c = \frac{9}{16}\sqrt{\frac{EG_c}{3l_0}}, \qquad \varepsilon_c = \sqrt{\frac{G_c}{3l_0E}} \tag{14}$$

From these expressions, we observed that the maximum stress will become infinite if l_0 becomes zero, which is consistent with the properties of Griffith's theory.

3. Numerical implementation

3.1. Monolithic scheme based on UEL

In this section, the displacement field and the phase-field are fully coupled and solved simultaneously. The weak forms of (10) are formulated as follows:

$$\int_\Omega(-\rho\ddot{\boldsymbol{u}}\cdot\delta\boldsymbol{u}-\boldsymbol{\sigma}:\delta\boldsymbol{\varepsilon})\mathrm{d}V + \int_{\Omega_t}\boldsymbol{t}^*\cdot\delta\boldsymbol{u}\mathrm{d}A = 0 \tag{15}$$

and

$$\int_\Omega -2(1-\phi)\delta\phi\mathcal{H}\mathrm{d}V + \int_\Omega G_c\left(l_0\nabla\phi\cdot\nabla\delta\phi+\frac{1}{l_0}\phi\delta\phi\right)\mathrm{d}V = 0 \tag{16}$$

The quadrilateral four-node element in 2D elements and the hexahedral eight-nodes in 3D elements are implemented to discretize the bulk domain Ω. The node values $\boldsymbol{u}_i$ and ϕ_i are discretized as follows:

$$\boldsymbol{u} = \sum_{i=1}^n N_i\boldsymbol{u}_i, \qquad \phi = \sum_{i=1}^n N_i\phi_i \tag{17}$$

where n is the total number of nodes per element. N_i denotes the shape function associated with node i. The corresponding matrices of the spatial derivatives can be expressed as:

$$\boldsymbol{B}_i^{\boldsymbol{u}} = \begin{bmatrix} N_{i,x} & 0 \\ 0 & N_{i,y} \\ N_{i,y} & N_{i,x} \end{bmatrix}, \qquad \boldsymbol{B}_i^\phi = \begin{bmatrix} N_{i,x} \\ N_{i,y} \end{bmatrix} \tag{18}$$

then it is possible to express the gradients:

$$\boldsymbol{\varepsilon} = \sum_{i=1}^n \boldsymbol{B}_i^{\boldsymbol{u}}\boldsymbol{u}_i, \qquad \nabla\phi = \sum_{i=1}^n \boldsymbol{B}_i^\phi\phi_i \tag{19}$$

According to (10) and (11), the contributions of one element at node i to the residual of the overall systems of equations are given as:

$$\boldsymbol{R}_i^u = \boldsymbol{F}_i^{\boldsymbol{u},\mathrm{ext}} - \boldsymbol{F}_i^{\boldsymbol{u},\mathrm{int}} - \boldsymbol{F}_i^{\phi,\mathrm{ine}} = \int_{\partial\Omega}N_i\boldsymbol{t}^*\mathrm{d}A - \int_\Omega\boldsymbol{B}_i^{\boldsymbol{u}}\boldsymbol{\sigma}\mathrm{d}V - \int_\Omega\rho N_i\ddot{\boldsymbol{u}}\mathrm{d}V$$
$$R_i^\phi = -F_i^{\phi,\mathrm{int}} = \int_{\Omega_e}2(1-\phi)N_i\mathcal{H} - G_c\left(l_0\left[\boldsymbol{B}_i^\phi\right]^T\nabla\phi+\frac{1}{l_0}N_i\phi\right)\mathrm{d}V \tag{20}$$

where $\boldsymbol{F}_i^{\boldsymbol{u},\mathrm{ext}}$ and $\boldsymbol{F}_i^{\boldsymbol{u},\mathrm{int}}$ denote the external forces and inner forces, respectively, which correspond to the displacement, whereas $F_i^{\phi,\mathrm{int}}$ can be explained as inner forces to the phase field. $\boldsymbol{F}_i^{\phi,\mathrm{ine}}$ represents the force of inertia. We used the Newton procedure to obtain the solutions by making $\boldsymbol{R}^u = 0$ and $R^\phi = 0$. The corresponding tangents on the element level can be obtained based on the inner forces:
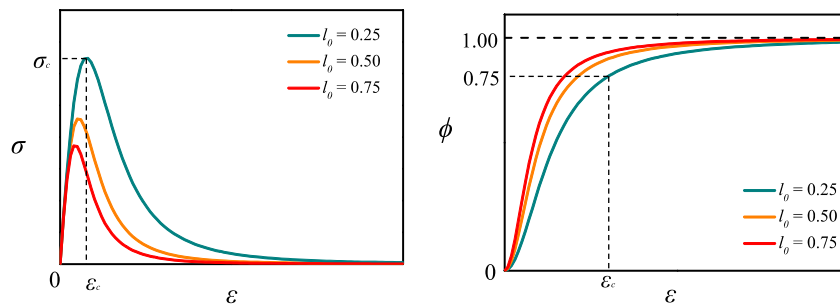

Fig. 2. One-dimensional stress–strain (a) and phase-field-strain curves (b) for the homogeneous solution with different l_0.

$$K_{ij}^{uu} = \frac{\partial F_{i,e}^{u,\text{int}}}{\partial u_j} = \int_\Omega \left[B_i^u\right]^T \frac{\partial \sigma}{\partial \varepsilon} \left[B_j^u\right] \mathrm{d}V$$

$$K_{ij}^{u\phi} = \frac{\partial F_{i,e}^{u,\text{int}}}{\partial \phi_j} = \int_\Omega \left[B_i^u\right]^T \frac{\partial \sigma}{\partial \phi} N_j \mathrm{d}V$$

$$K_{ij}^{\phi u} = \frac{\partial F_{i,e}^{\phi,\text{int}}}{\partial u_j} = \int_\Omega -2(1-\phi)N_i\left[\frac{\partial \mathcal{H}}{\partial \varepsilon}\right]\left[B_j^u\right] \mathrm{d}V \qquad (21)$$

$$K_{ij}^{\phi\phi} = \frac{\partial F_{i,e}^{\phi,\text{int}}}{\partial \phi_j} = \int_\Omega \left(\left[B_i^\phi\right]^T G_c l_0 \left[B_j^\phi\right] + N_i\left(2\mathcal{H}+\frac{G_c}{l_0}\right)N_j\right)\mathrm{d}V$$

$\partial\sigma/\partial\varepsilon$ represents the fourth-order tensor:

$$\begin{aligned}\frac{\partial\sigma}{\partial\varepsilon} &= \frac{\partial}{\partial\varepsilon}\left(\left[(1-\phi)^2+\kappa\right]\frac{\partial\psi^+}{\partial\varepsilon}+\frac{\partial\psi^-}{\partial\varepsilon}\right)\\ &= \left[(1-\phi)^2+\kappa\right]\left(\lambda H(\mathrm{tr}(\varepsilon)\mathbb{J}+2\mu)\mathbb{P}^+\right)\\ &\quad +\left(\lambda H(-\mathrm{tr}(\varepsilon)\mathbb{J}+2\mu)\mathbb{P}^+\right)\end{aligned} \qquad (22)$$

where $H(x)$ is the Heaviside function. $\mathbb{J}$ is a fourth-order tensor such that if $i = k$ and $j = l$, the result is unity, and if one of the equalities is violated, then the result is zero. Projection tensors $\mathbb{P}^\pm$ can be expressed based on [39]:

$$\mathbb{P}^\pm = \sum_a^d \left(H(\pm\varepsilon_a)\mathbb{Q}_a + \sum_{b,b\neq a}^d \frac{\langle\varepsilon_a\rangle_\pm}{2(\varepsilon_a-\varepsilon_b)}(\mathbb{G}_{ab}+\mathbb{G}_{ba})\right) \qquad (23)$$

with

$$\begin{aligned}\mathbf{M}_a &= \mathbf{n}_a \otimes \mathbf{n}_a\\ (\mathbb{Q}_a)_{ijkl} &= (\mathbf{M}_a)_{ij}(\mathbf{M}_a)_{kl}\\ (\mathbb{G}_{ab})_{ijkl} &= (\mathbf{M}_a)_{ik}(\mathbf{M}_b)_{jl}+(\mathbf{M}_a)_{il}(\mathbf{M}_b)_{jk}\end{aligned} \qquad (24)$$

$\partial\sigma/\phi$ and $\partial\mathcal{H}/\varepsilon$ are given as:

$$\frac{\partial\sigma}{\partial\phi} = -2(1-\phi)\left(\lambda\langle\mathrm{tr}(\varepsilon)\rangle_+\mathbf{1}+2\mu\varepsilon_+\right), \qquad \frac{\partial\mathcal{H}}{\partial\varepsilon} = \lambda\langle\mathrm{tr}(\varepsilon)\rangle_+\mathbf{1}+2\mu\varepsilon_+ \qquad (25)$$

Furthermore, the implicit Hughes–Hibert–Taylor (HHT) time integration is adopted in dynamic calculations; hence, the residual force vectors are re-written as:

$$\begin{aligned}R_{i,t+\Delta t}^u &= F_{i,t+\Delta t}^{u,\text{ext}} - F_{i,t+\Delta t}^{u,\text{ine}} - (1+\alpha)F_{i,t+\Delta t}^{u,\text{int}} + \alpha F_{i,t}^{u,\text{int}}\\ R_{i,t+\Delta t}^\phi &= -(1+\alpha)F_{i,t+\Delta t}^{\phi,\text{int}} + \alpha F_{i,t}^{\phi,\text{int}}\end{aligned} \qquad (26)$$

where α is the HHT integration operator with values of $(-1/3, 0)$, and $\Delta t = t_{n+1} - t_n$ is the time step size. By neglecting the material damping effect, the tangent matrix of one element is:

$$\begin{aligned}S_{ij} &= M_{ij}\frac{\mathrm{d}\ddot{u}}{\mathrm{d}u} + (1+\alpha)K_{ij}\\ \frac{\mathrm{d}\ddot{u}}{\mathrm{d}u} &= \frac{1}{\beta\Delta t^2}, \quad \beta = \frac{(1-\alpha)^2}{4}\end{aligned} \qquad (27)$$

The above procedures on the element level have been implemented in the Abaqus standard using a UEL subroutine called for each iteration in a given increment. The plotting of the results of the user elements is not supported in Abaqus/CAE. One of the choices is to overlay standard elements on the user elements, but the computation time would be approximately doubled. Therefore, the results of the user elements are extracted to an external visualization software (e.g., Tecplot) using a UEXTERNALDB subroutine.

3.2. Staggered schemes based on UMAT/VUMAT

In this section, we obtained the phase field and the displacement field sequentially based on the operator splits proposed by Miehe et al. [25]. For the staggered solution strategy, the two fields

are solved independently so that both the implicit and explicit schemes can be used to solve the equation of motion.

In the implicit analysis, the procedure of solving displacement is the same as what has been described in Section 3.1 for K^{uu} and R^u. Before that, the linear phase-field evolution equation in (10) should be solved using the efficient direct method:

$$\phi = F^\phi \left[K^{\phi\phi}\right]^{-1} \qquad (28)$$

F^ϕ on an element level is:

$$F_i^\phi = \int_\Omega 2N_i\mathcal{H}\mathrm{d}V \qquad (29)$$

A UMAT subroutine is used to exchange the local history field $\mathcal{H}$ and the phase field ϕ on integration points. Moreover, the stress σ and the consistent tangent modulus $\partial\sigma/\partial\varepsilon$ need to be updated in each iteration in the UMAT subroutine.

In the explicit analysis, the displacement field is solved using the explicit central-difference time-integration method:

$$\begin{aligned}u_{i,t+\Delta t} &= u_{i,t} + \dot{u}_{i,t+1/2\Delta t}\Delta t\\ \dot{u}_{i,t+1/2\Delta t} &= \dot{u}_{i,t-1/2\Delta t} + \ddot{u}_{i,t}\Delta t\end{aligned} \qquad (30)$$

and

$$\ddot{u}_i = (M_{ij})^{-1}\left(F_i^{u,\text{ext}} - F_i^{u,\text{int}}\right) \qquad (31)$$

While the phase field can also be solved directly using the equation (28). We used a VUMAT subroutine to exchange the local history field $\mathcal{H}$ and the phase field ϕ on integration points. Note that only the stress σ needs to be updated in each increment in the VUMAT subroutine.

The local history field, the phase field, and the displacement field are updated sequentially in the staggered scheme, so the nonlinearity is obviously reduced compared with the monolithic scheme. Besides, the staggered scheme provides a better use of Abaqus by allowing the results post-processing by reducing the computation cost.

4. Numerical examples

By performing numerical examples, we investigated the performance of the different solution schemes for different benchmarks under different loadings states "quasi-static and dynamic using implicit and explicit approaches." We compared the phase-field model with the XFEM in linear elastic fracture mechanics (LEFM). We solved the simulations using the thread-parallel execution and mutexes that were adopted from the parallelization solvers of Abaqus. For both solution schemes, we examined the solution of a coupled system with different numbers of CPUs. Moreover, we studied the length-scale parameter l_0 in a dynamic case with the presence of the experimental results. For the examples below, the parameter κ is set to a small quantity in all examples to prevent system ill-conditioning. The effective element sizes are computed as $h = \sqrt[d]{a}$, where a is the area of an element in two dimensions and the volume of an element in three dimensions.

4.1. 2D symmetric three-point bending-beam test

This test is designed for comparing the phase-field model with the XFEM based on LEFM. Fig. 3 shows the geometric setup and loading conditions. The material parameters are $E = 37$ GPa, $v = 0.2$, and $G_c = 42.6$ J/m^2 with plane strain conditions. The length scale l_0 is chosen to be 0.01 m and 0.001 m, respectively. The discretization is refined in the expected crack-propagation zone, and the effective element size $h \approx l_0/4$. The
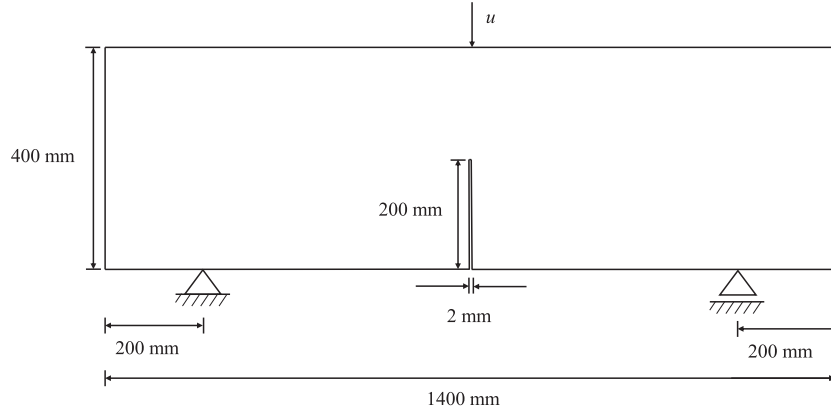
Fig. 3. Symmetric three-point bending test. Geometry and boundary conditions.

quasi-static monolithic solver is chosen to guarantee the solution accuracy.

We adopted the built-in solution scheme of Abaqus for the XFEM based on LEFM [40]. We used the maximum principal stress criterion for crack initiation before the crack is governed by LEFM. The material parameters and meshes are the same as those used for the phase-field model. For XFEM, we calculated the maximum stress for crack initiation using Eq. (14) with $l_0 = 0.01$ m.

Fig. 4 compares the phase-field and XFEM cracks at different load steps. The load-CMOD (Crack Mouth Opening Displacement) curves are shown in Fig. 5. Blue and red colors correspond to the undamaged and the fully cracked material for the phase-field crack, while the displacement discontinuities represent the crack for XFEM. We observed that the reaction force based on the XFEM is closer to the one calculated by the phase-field model with $l_0 = 0.01$ m because it corresponds to the critical stress for crack initiation in the XFEM.

4.2. 2D single-edge notched tension test

In this example, we adopted a square plate with a horizontal notch placed from $(x = 0, y = 0.5)$ to $(x = 0.5, y = 0.5)$ of the specimen, as given in the geometry in Fig. 6. The boundary conditions are $u_y = 0$ and traction free in the x-direction, whereas the left and right boundaries $(x = 0$ and $x = 1.0)$ are $u_x = 0$ and traction free in the y-direction. The loading displacement is applied in the y-direction at $y = 1.0$, where this edge is fixed in the x-direction.
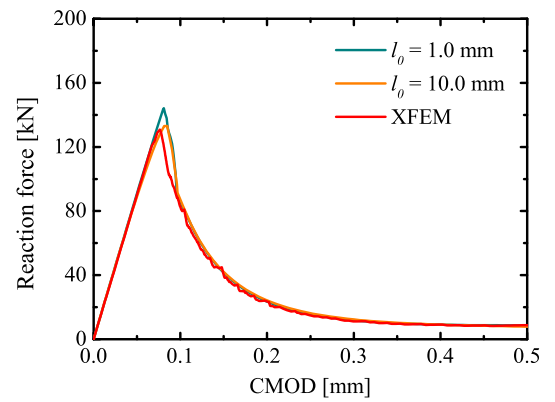
Fig. 5. Load-CMOD curves for symmetric three point bending test.

The initial crack is modeled as a displacement discontinuity by duplicated nodes. The model is discretized with 256×256 uniform four-node plane-stress elements. The material properties are $E = 210$ GPa, $v = 0.2$, and $G_c = 2700$ J/m^2.

The length scale l_0 is chosen as 0.0150 mm and 0.0075 mm, respectively. For the staggered schemes, monotonic displacement increments $\Delta u = 1 \times 10^{-4}$ mm were applied in the first 50 time steps. We considered three cases with different loading increments in the remaining time steps: $\Delta u = 1 \times 10^{-5}$ mm,
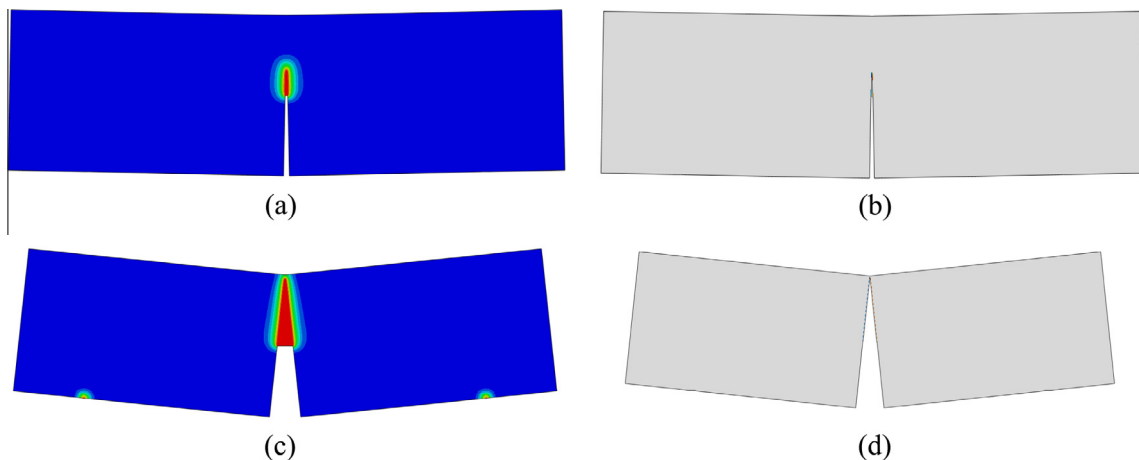

Fig. 4. Crack patterns of phase-field model with l0 = 0.01 m and XFEM: (a) phase-field crack with $u = 0.11$ mm, (b) XFEM crack with $u = 0.11$ mm, (c) phase-field crack with $u = 0.50$ mm, and (d) XFEM crack with $u = 0.50$ mm.
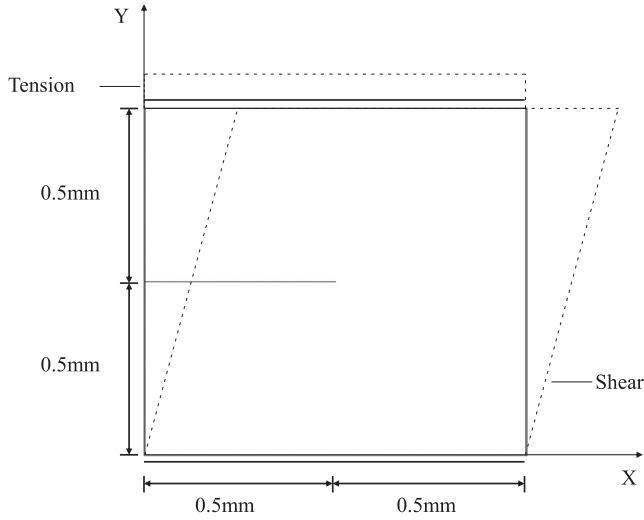
Fig. 6. Geometry and boundary conditions for the static tension and shear problems.

$\Delta u = 1 \times 10^{-6}$ mm, and $\Delta u = 1 \times 10^{-7}$ mm. We adopted the automatic loading step sizes for the monolithic scheme.

Fig. 7 compares the crack patterns for the monolithic and staggered schemes at the same loading level, and the load–displacement curves are shown in Fig. 8. As illustrated in the figure, the staggered scheme delays the crack-initiation time, but this behavior can be improved by reducing the load increments. The reaction–force curves of the different approaches are also converged. The load–displacement curve with $\Delta u = 1 \times 10^{-5}$ mm is in good agreement with the results reported by Hesch and Weinberg [30], in which the same meshes and loading increments were used.

4.3. 2D single-edge notched shear test

In this test, we examined the same geometry and mesh in Fig. 6 with different loading modes. We applied the pure shear loading on the specimen. The boundary conditions of the specimen are $u_x = 0$ and $u_y = 0$ at $y = 0$, $u_y = 0$ and traction free in the

x-direction at the edges ($x = 0$ and $x = 1.0$). The upper end ($y = 1.0$) is subjected to a displacement traction in the x-direction, whereas $u_y = 0$.

The same geometry and properties of the tension test specimen. For the staggered scheme, monotonic displacement increments of $\Delta u = 1 \times 10^{-4}$ mm are applied in the first 50 time steps. In addition, we considered three different loading increments in the remaining time steps: $\Delta u = 1 \times 10^{-4}$ mm, $\Delta u = 1 \times 10^{-5}$ mm, and $\Delta u = 1 \times 10^{-6}$ mm. Meanwhile, we adopted the automatic loading step sizes for the monolithic scheme.

Fig. 9 examines the crack patterns for the monolithic and staggered schemes at the same loading steps. The load–displacement curves are shown in Fig. 10. As expected, the staggered scheme delays the crack evolution, and the situation is improved by reducing the load increments. The test behavior exhibits the same conclusion as the tension test. We obtained good agreement compared to the monolithic solution when the loading increments are sufficiently small. It should be noted that the staggered and monolithic schemes have almost the same crack patterns when $\Delta u = 1 \times 10^{-6}$ mm is adopted with $l_0 = 0.0075$ mm. Furthermore, the load–displacement curve with $\Delta u = 1 \times 10^{-5}$ mm is in agreement with the results reported by Hesch and Weinberg [30], in which the same meshes and loading increments were used.

4.4. 3D single-edge notched tension test

In this example, we present the model for single-edge notched tension in 3D. We used the geometry setup in Section 4.2 with a thickness of 0.1 mm. The material parameters are identical to the corresponding 2D example, and $u_z = 0$ is applied on the bottom, left, and right faces. The other boundary conditions are identical. The specimen is discretized with 96,896 linear hexahedral elements refined in an area in which the crack is expected to propagate. For the staggered scheme, monotonic displacement increments of $\Delta u = 1 \times 10^{-4}$ mm are applied in the first 50 time steps, while we considered two cases with different loading increments in the remaining time steps: $\Delta u = 1 \times 10^{-5}$ mm and $\Delta u = 1 \times 10^{-6}$ mm. We adopted the automatic loading step sizes for the monolithic scheme.
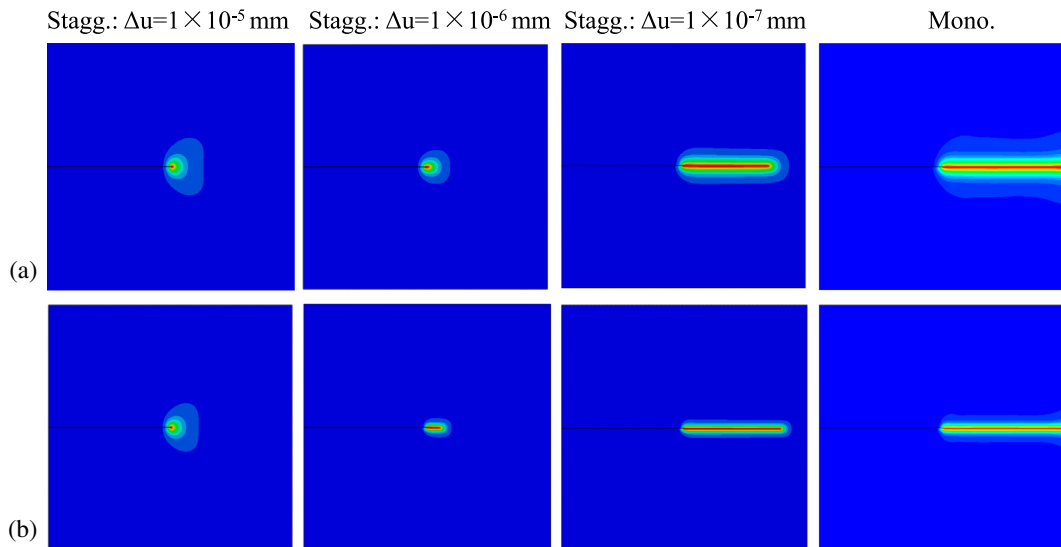

Fig. 7. Crack patterns of the staggered and monolithic schemes for 2D single-edge notched tension test: (a) $u = 5.29 \times 10^{-3}$ mm for a length scale of $l_0 = 0.0150$ mm and (b) $u = 5.54 \times 10^{-3}$ mm for a length scale of $l_0 = 0.0075$ mm.
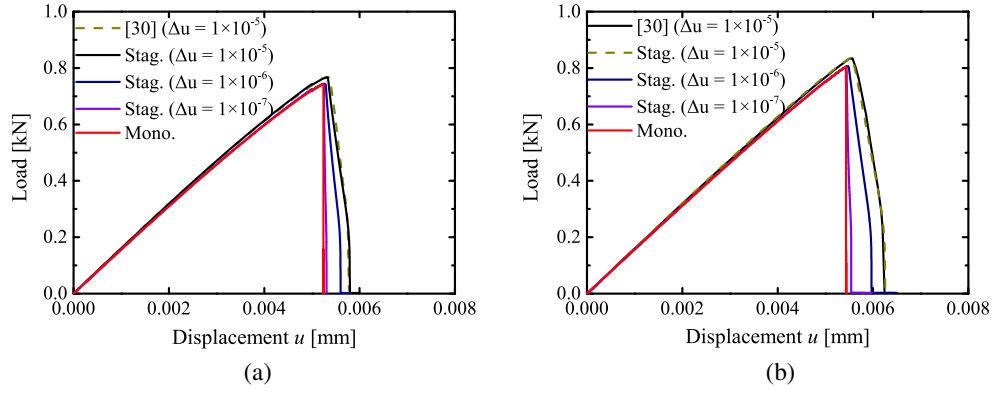
Fig. 8. Load–displacement curves of the different schemes for 2D single-edge notched tension test: (a) l_0 = 0.0150 mm and (b) l_0 = 0.0075 mm.
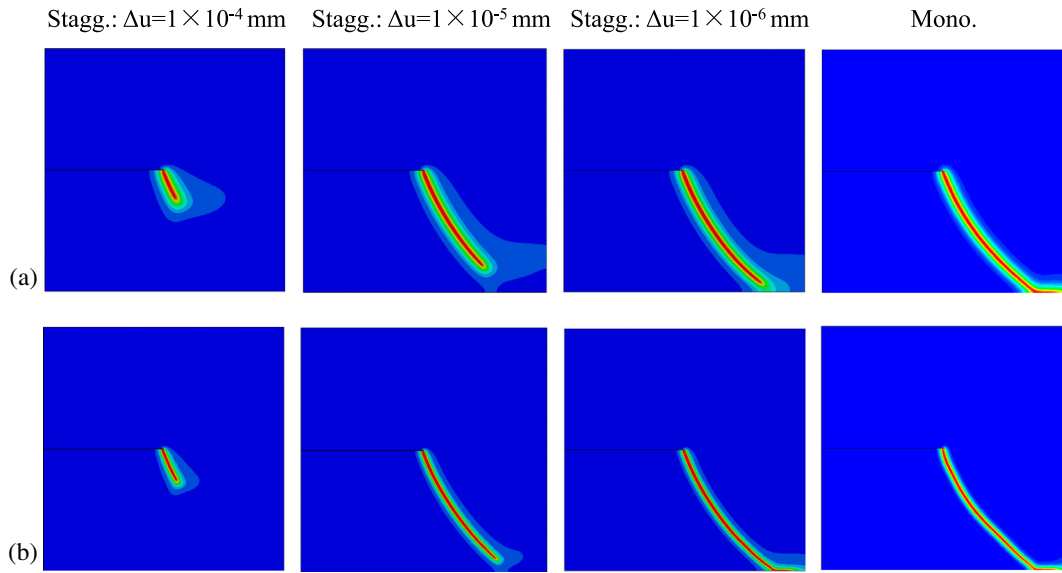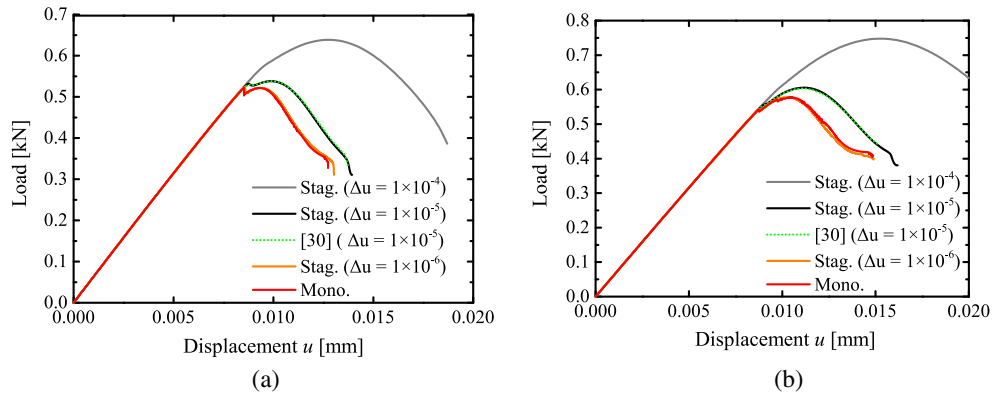

Fig. 9. Crack patterns of the staggered and monolithic schemes for the 2D single-edge notched shear test: (a) $u = 12.95 \times 10^{-3}$ mm for a length scale of l_0 = 0.0150 mm and (b) $u = 15.08 \times 10^{-3}$ mm for a length scale of l_0 = 0.0075 mm.

Fig. 10. Load–displacements curves of the staggered and monolithic schemes for 2D single-edge notched shear test: (a) l_0 = 0.0150 mm and (b) l_0 = 0.0075 mm.

The results of the crack patterns, $\phi \geqslant 0.95$, for the same loading steps of both solution schemes and the length scale l_0 = 0.00150 mm are shown in Fig. 11. The load–deflection curves are presented in Fig. 12. The computation time for the staggered scheme with $\Delta u = 1 \times 10^{-6}$ mm is almost equal to that of the monolithic scheme.

4.5. 2D dynamic crack branching

To investigate the potential of the phase-field method to capture dynamic crack branching, we modeled a pre-notched brittle plate under an impact stress $\sigma_y = 1$ MPa at the top and bottom surfaces ($y = \mp 20$) in Fig. 13. The material properties are
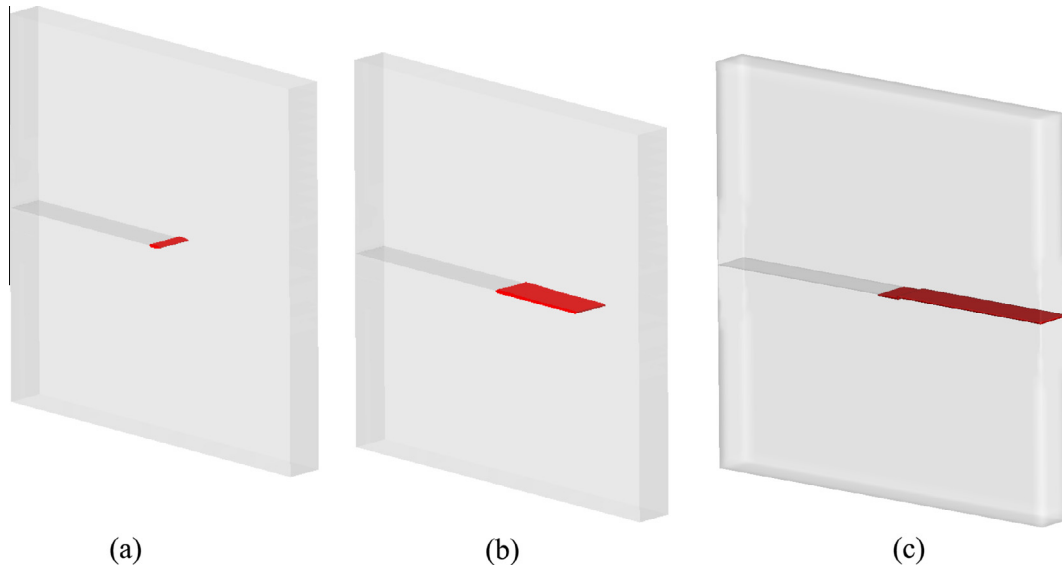
Fig. 11. Crack patterns at $u = 6.25 \times 10^{-3}$ mm between the staggered and monolithic schemes for 3D single-edge notched shear test: (a) $\Delta u = 1 \times 10^{-5}$ mm in the staggered scheme, (b) $\Delta u = 1 \times 10^{-6}$ mm in the staggered scheme, and (c) automatic load increments in the monolithic scheme.
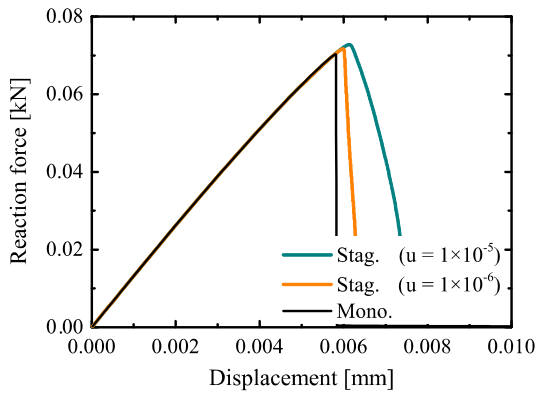

Fig. 12. Load–displacement curves of the staggered and monolithic schemes for the 3D single-edge notched shear test.
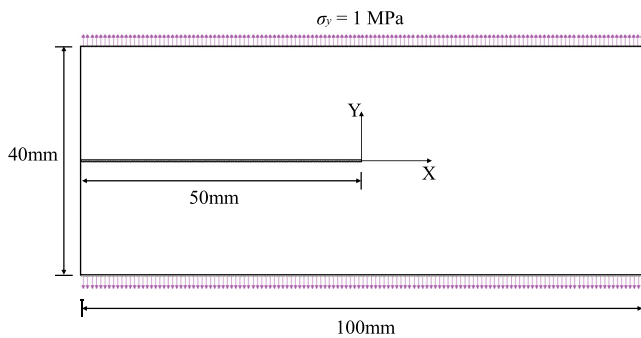

Fig. 13. Geometry and boundary conditions for the dynamic crack-branching problem.

$\rho = 2450$ kg/m^3, $E = 32$ GPa, $v = 0.2$, and $G_c = 3$ J/m^2. The Rayleigh wave speeds are $v_R = 2125$ m/s. We made the initial 2.5×10^{-4} m wide crack based on geometry, and we set the length scale to $l_0 = 5.0 \times 10^{-4}$ m.

Borden et al. [26] and Schlütter et al. [23] simulated the same problem with different decompositions for the elastic energy density. In [23,26] the simulations were solved using the monolithic

scheme. In this example, we used both the monolithic and staggered schemes by incorporating two different meshes of four-node plane strain elements. We used the HHT time integration with $\alpha = -0.05$ for both schemes. The time step is chosen as $\Delta t = 1 \times 10^{-7}$ s for the monolithic scheme and $\Delta t \approx h/v_R$ for the staggered scheme.

Fig. 14 shows the results for the phase field at 80 µs. In the monolithic scheme, mesh 1 with $h = 2.50 \times 10^{-4}$ m ($l_0 = 2h$) and mesh 2 with $h = 1.25 \times 10^{-4}$ m ($l_0 = 4h$) have similar crack patterns, although the crack in mesh 1 fails to reach the boundary, as in mesh 2. Mesh 1 in the staggered scheme clearly delays the crack branching, while mesh 2 makes up for it to some extent. As we can see, the diffusive crack is wider in a coarse mesh or in a staggered scheme.

The above phenomenon can be explained by the evolution of the potential energy differences, as shown in Fig. 15. Fig. 15(a) shows the elastic energy defined by Eq. (6), and Fig. 15(b) shows the crack surface energy defined by Eq. (3). The plots illustrate that the cracks in the staggered scheme have a larger deformation energy and dissipated energy compared with those in the monolithic scheme. The reason for the differences is that the solution in the staggered scheme is not fully converged at each time step, although small time steps can be used to remedy it to some degree.

Fig. 16 depicts the crack-tip velocity obtained from postprocessing the results. Because the phase field represents the crack topology as the diffusive contours, the crack tip is assumed at the contour line with $\phi = 0.85$ when calculating the crack velocity. The curves are similar and have almost the same time for crack branching, except for the one from mesh 1 in the staggered scheme. We note that crack branching occurs between 34 µs and 37 µs with a velocity of $0.49 v_R$. This is in fairly good agreement with the result reported in [26]. Fig. 17 plots the Max. Principal stress at 70 µs, and it illustrates that the staggered scheme can exhibit similar results with the monolithic scheme if a finer mesh is adopted.

4.6. 2D simulation of the Kalthoff test

In the classic Kalthoff experiment, a double pre-notched steel plate is impacted by a projectile with an initial velocity v_0. The test is often used as a standard example to test the accuracy of the numerical methods in order to model the dynamic crack propaga-
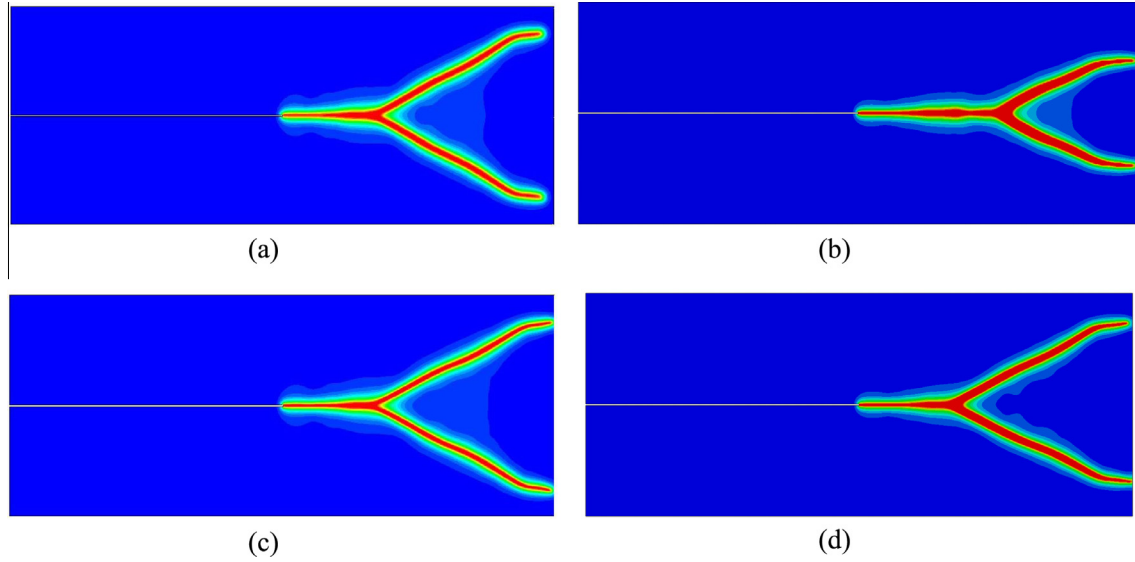
Fig. 14. Phase field for the crack-branching example at $t = 80$ µs: (a) mesh 1 in the monolithic scheme, (b) mesh 1 in the staggered scheme, (c) mesh 2 in the monolithic scheme, and (d) mesh 2 in the staggered scheme.
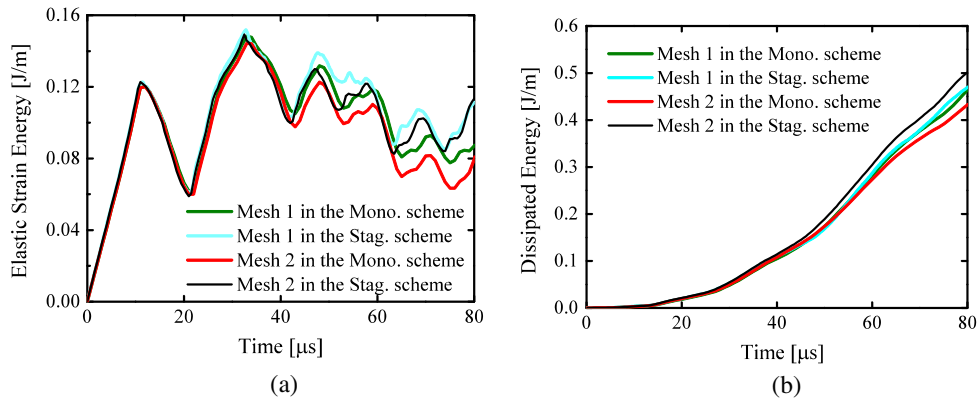

Fig. 15. The potential energy curves for the crack-branching example: (a) the elastic energy and (b) the dissipated energy.
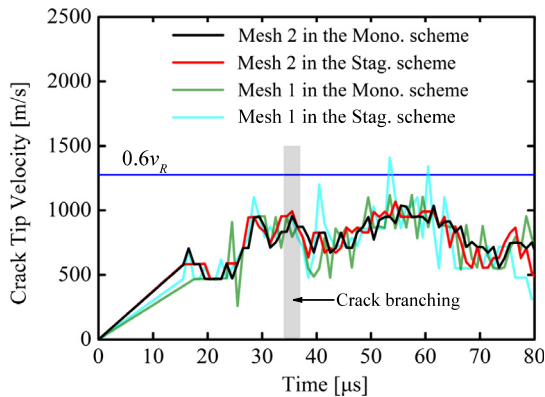

Fig. 16. Crack-tip velocity curves for the crack-branching example.

tion. This example has been solved by using the phase-field model in the staggered scheme in [28,30]. Here, we model it using both schemes and compared the results.

The sample geometry and boundary conditions are given in Fig. 18. The imposed initial velocity v_0 increases linearly with time to $t_0 = 1$ µs, and then holds at $v_0 = 16.5$ m/s. The material param-

eters are $\rho = 8000$ kg/m^3, $E = 190$ GPa, $v = 0.3$, and $G_c = 2.213 \times 10^4$ J/m^2. The Rayleigh wave speed is $v_R = 2803$ m/s. The initial crack is placed as a displacement discontinuity using duplicated nodes. The length scale is set to $l_0 = 3.9 \times 10^{-4}$ m, and we used the HHT time integration with $\alpha = -0.05$ for the monolithic scheme, while we adopted the explicit central-difference time integration for the staggered scheme. For the time step, we chose $\Delta t = 5 \times 10^{-8}$ s for the monolithic scheme. The explicit time integration is conditionally stable and the time increment size is determined by the smallest element size and the material wave speed [41].

Fig. 19 shows the crack patterns at 87 µs. In the monolithic scheme, mesh 1 with $h = 1.95 \times 10^{-4}$ m ($l_0 = 2h$) and mesh 2 with $h = 9.75 \times 10^{-5}$ m ($l_0 = 4h$) have almost the same crack patterns. For the staggered scheme, the crack in mesh 1 failed to reach the top end with the critical time step $\Delta t = 3 \times 10^{-8}$ s. The crack in mesh 2 with the critical time step $\Delta t = 1.5 \times 10^{-8}$ s is almost the same as in the monolithic scheme. The average angle of the crack for mesh 2 in the two schemes is 68°, which is in good agreement with the experimental results for a crack propagation angle of 70°. Fig. 20 shows the evolution of the potential energy. In addition, the results confirm that the staggered schemes are affected more by the element size. Fig. 21 depicts the crack-tip velocity with the
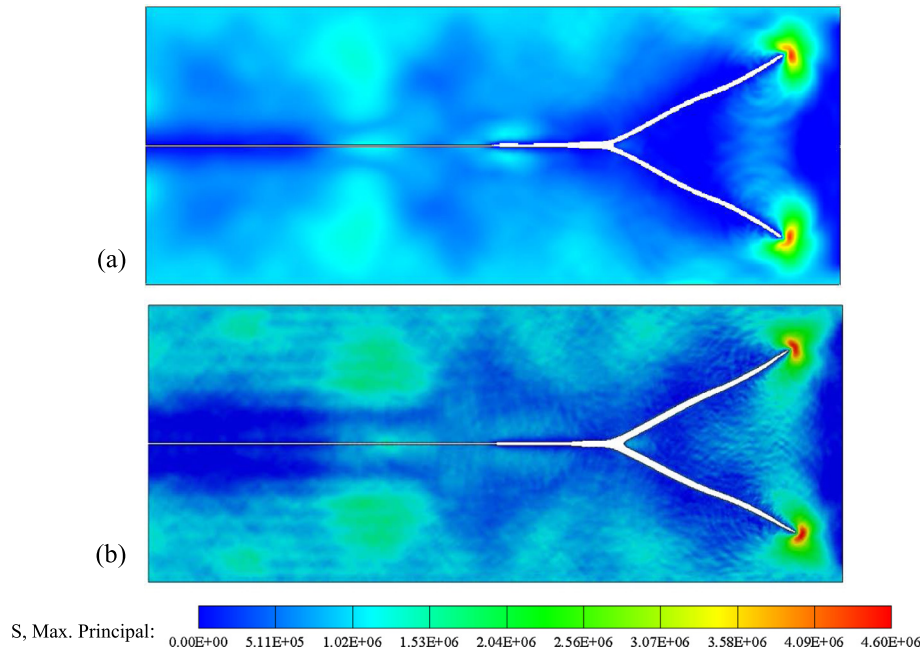
Fig. 17. Max. principle stress for mesh 2 at $t = 70$ μs, where $\phi > 0.95$ has been removed from the plot.
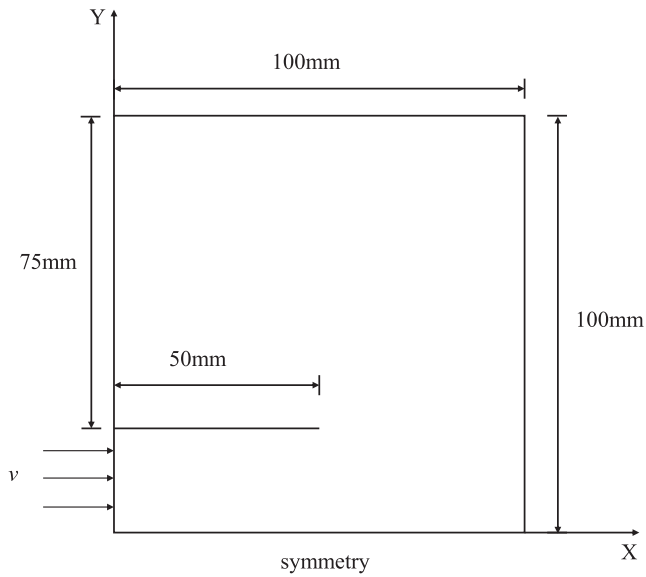

Fig. 18. Geometry and boundary conditions for the Kalthoff test.

Fig. 19. Results of phase field for the 2D Kalthoff test at $t = 87$ μs: (a) mesh 1 in the monolithic scheme, (b) mesh 1 in the staggered scheme, (c) mesh 2 in the monolithic scheme, and (d) mesh 2 in the staggered scheme.

same assumption as the previous case. It is clear that the crack propagates slower in mesh 1 in the staggered scheme. The maximum crack-tip velocity for mesh 2 is about $0.55\,v_R$. Fig. 22 shows the maximum principle stress for mesh 2, and it is very similar in both schemes.

The critical time step for mesh 1 is reduced by a factor of 10 $\left(\Delta t = 3 \times 10^{-9}\,\text{s}\right)$, but it has almost the same crack patterns. As a result, we believe that finer meshes (e.g. $h \leqslant l_0/4$) are also needed for a staggered scheme in dynamic problems.

4.7. 3D dynamic crack branching

Dynamic fracture experiments of the concrete compact tension specimen (CTS) were reported in [42], and the experiments were
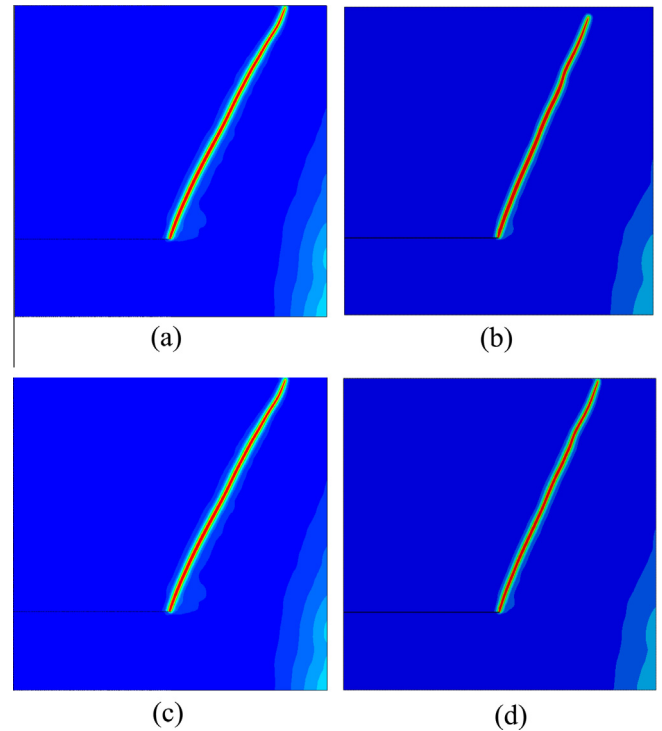
simulated by the micro-plane model [42,43]. Crack branching will occur when the loading rates reach some high values.

Next, we introduce the modeling of the benchmark in the phase field. The dimensions of the concrete specimen are $200 \times 200 \times 25$ mm, and the notch length and width are 64 and 18 mm, respectively. The specimen is fastened in two steel frames, and the contact surfaces are glued tightly. The material parameters of the concrete specimen are $\rho = 2400$ kg/m³, $E = 36$ GPa, $v = 0.18$,
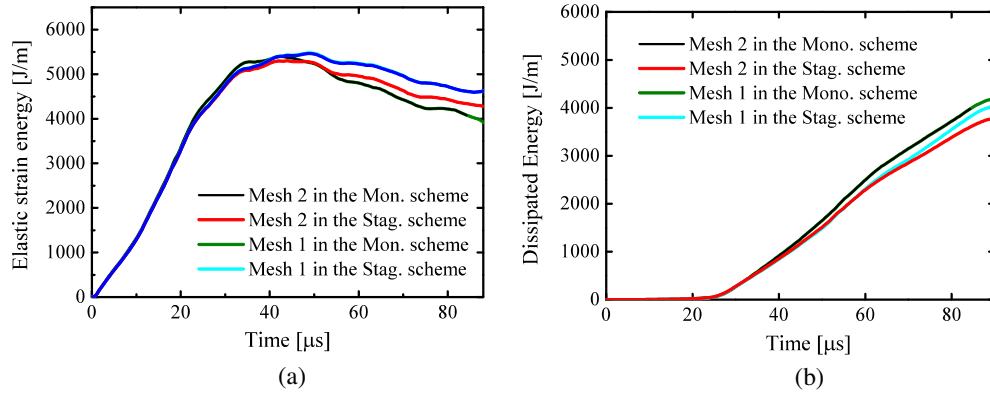
Fig. 20. The potential energy curves for the 2D Kalthoff test: (a) the elastic energy and (b) the dissipated energy.

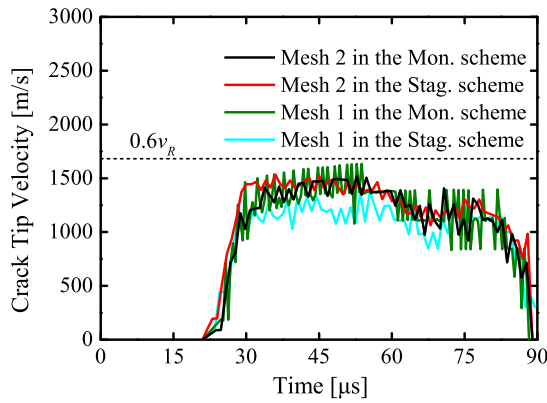**Fig. 21.** The crack-tip velocity curves for the 2D Kalthoff test.

and $G_c = 65$ J/m². The material properties of the steel frames are $\rho = 8000$ kg/m³, $E = 210$ GPa, and $v = 0.33$. The specimen is discretized with 51,476 linear hexahedral elements refined in the lower half part (see Fig. 23). The length of the effective element edge is 1.25 mm. The steel frame is fixed from the top in the y direction, and the bottom of the steel frame is subjected to displacement loading. The contacts between the concrete specimen and the steel frames are connected through surface-node tie constraints [40].

We adopted the explicit staggered scheme with a loading rate of 3.3 m/s. The critical time step is $\left(\Delta t = 1.2 \times 10^{-7} \text{ s} \right)$. The concrete tensile strength $f_t = 3.80$ MPa [42], and the length scale parameter is determined as $l_0 = 17.1$ mm from Eq. (14). Fig. 24(a) shows the crack patterns, $\phi \geqslant 0.99$, and it is consistent with the experimental results. However, the crack is too diffusive with respect to the concrete specimen. Fig. 24 (b) and (c) shows that the crack size is decreasing as l_0 decreases. The reaction force curves are compared with the experiment data [42] in Fig. 25. We can see that the result from $l_0 = 17.1$ mm is the closest to the measured data. The results again illustrate that Eq. (14) can reveal the link between the tensile strength and regularization length l_0. Moreover, decreasing l_0 causes an increase in the peak reaction force with thinner cracks. In conclusion, a larger specimen should be considered when the phase-field model is used for concrete simulations. A similar conclusion is also reported in [44].

4.8. 3D crack propagation

To demonstrate the ability of the phase-field model to predict crack propagation in three-dimensional space, a concrete block hit by a rigid cylindrical body with an initial velocity is simulated in the final example, see Fig. 26. Considering the symmetry of the problem, only one quarter of the specimen is considered. The cylindrical rigid body is tight to the concrete block by using
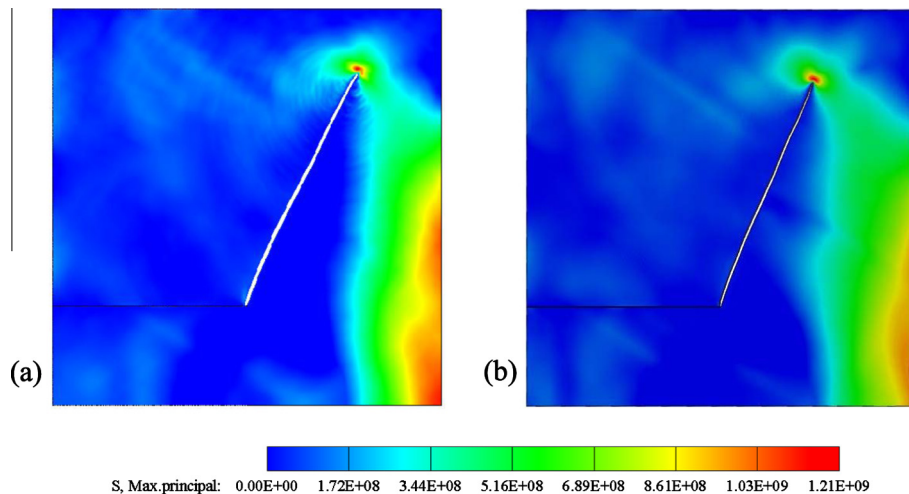

Fig. 22. Max. Principle stress for mesh 2 at $t = 70$ μs, where $\phi > 0.95$ have been removed from the plot: (a) mesh 2 in the monolithic scheme and (b) mesh 2 in the staggered scheme.
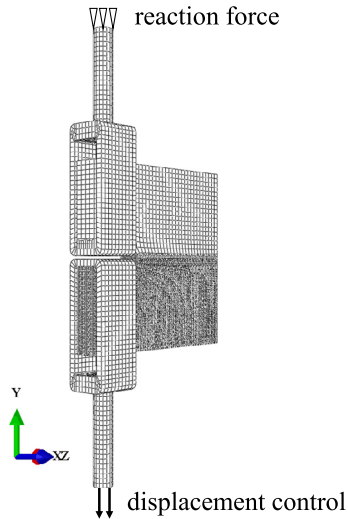
Fig. 23. Finite element for the 3D dynamic crack-branching test.

Fig. 25. Measured and numerically predicted reaction-time response for the 3D dynamic crack branching test.

surface–surface contact and adopting the kinematic contact method of Abaqus [40].

The material parameters are $\rho = 2400\ \mathrm{kg/m^3}$, $E = 36\ \mathrm{GPa}$, $v = 0.18$, and $G_c = 65\ \mathrm{J/m^2}$. The concrete block is discretized with 148,137 uniform linear hexahedral elements and l_0 equals to 4.0 mm. The imposed initial velocity for the rigid body v_0 rises linearly with time $t_0 = 1\ \mu s$, and then holds at $v_0 = 5\ \mathrm{m/s}$.

Symmetric boundary conditions are applied on the symmetrical surfaces, while the other surfaces are free. Fig. 27 shows the crack patterns at different times with $\phi \geqslant 0.99$. The cracks form at time $t_0 = 30\ \mu s$. Then, the crack propagates with an average angle of 58°. At the same time, the stress waves reach the bottom and reflect at the boundaries. The waves cause the break of the lower part before touching the cracks.

5. Parallel computing of phase-field model

We examined several aspects involved in the implementation of the phase-field model using the finite-elements method in parallel computers with local memory. In particular, we compared the costs of implementing the model using partially coupled and fully coupled iterative solvers for serial and parallel CPUs, which solve the linear systems that occur.
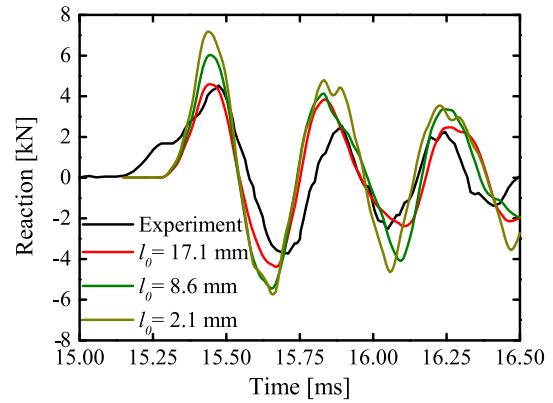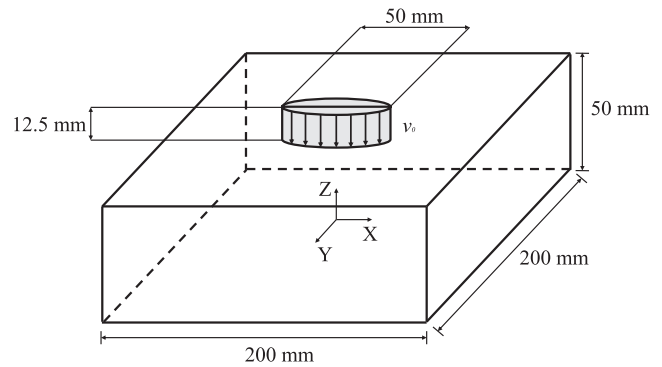

Fig. 26. Geometry for the 3D crack-propagation test.

The analysis in parallel computers provides a natural way of increasing the efficiency compared to the serial implementation. For implicit Newton's method, it is also known that increasing the number of CPUs does not imply a reduction in the computation time, and optimization is needed in this regard. The benchmark presented in 4.2 is used for this investigation. The results in Fig. 28 reveal that the solution time is reduced by 51% in the fully coupled scheme when we use 4 CPUs, and this time varies with the number of CPUs. Generally, the staggered scheme acts the same when $(\Delta u = 1 \times 10^{-6}\ \mathrm{mm})$. In the case of $(\Delta u = 1 \times 10^{-7}\ \mathrm{mm})$,
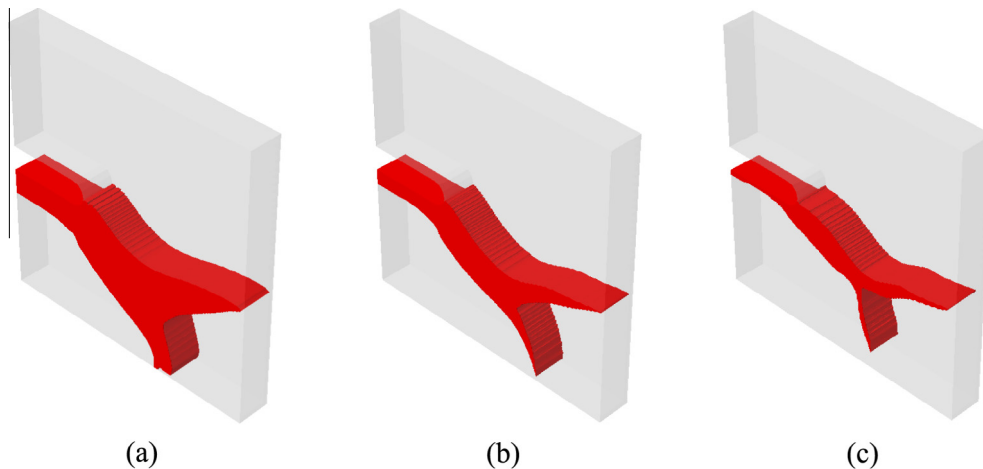

Fig. 24. Results of phase field for the 3D dynamic crack-branching test: (a) l_0 = 17.1 mm, (b) l_0 = 8.6 mm, and (c) l_0 = 2.1 mm.

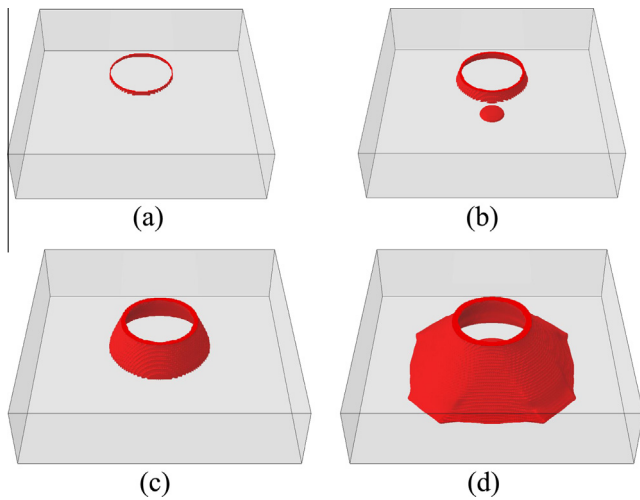**Fig. 27.** Results of phase field for the 3D crack-propagation test: (a) $t = 30$ μs, (b) $t = 35$ μs, (c) $t = 45$ μs and (d) $t = 75$ μs.
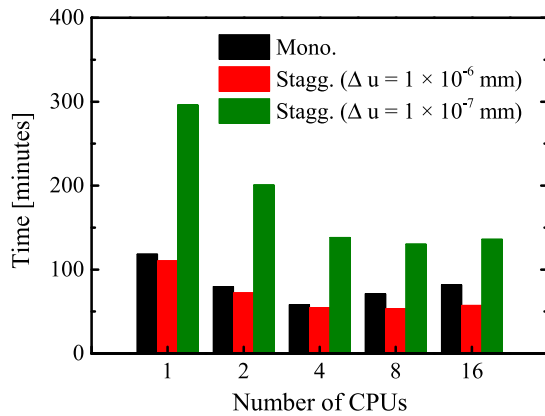

Fig. 28. Time versus the number of CPUs.

the shorter time for the solution was obtained with 8 CPUs. Note that this time is already more than twice that of ($\Delta u = 1 \times 10^{-6}$ mm). In conclusion, the fully coupled scheme and staggered scheme need the same number of CPUs for specific load increments, but the staggered scheme will need to employ more CPUs for very small load increments that are required for increased solution accuracy.

6. Conclusions

In this paper, we presented procedures for the implementation of the monolithic and staggered schemes of the phase-field model using UEL and UMAT/VUMAT subroutines of Abaqus. The monolithic scheme solved the phase-field and the displacement simultaneously, and it has a higher accuracy with higher computation cost. The staggered scheme is more efficient, whereby the equations of motion could be handled using both the implicit Newton iteration and explicit central-difference time integration rule.

We compared the monolithic scheme with the staggered scheme by considering different scenarios. The results showed that the staggered scheme is more sensitive to the element size, and it requires finer meshes to realize the correct crack patterns in dynamic problems. We investigated the influence of the length-scale parameter of the crack. Note that the parameter can be eval-

uated through its relationship with the critical stress derived in a one-dimensional (1D) problem although the relationship has no rigorous proof in two or three dimensions. Finally, we illustrated the potential of the phase-field model to handle crack propagation in 3D spaces.

Acknowledgements

References

[1] T. Belytsclil, H. Chen, J. Xu, G. Zi, Int. J. Numer. Meth. Eng. 58 (2003) l873–l905.
[2] C. Linder, F. Armero, Finite Elem. Anal. Des. 45 (4) (2009) 280–293.
[3] T. Menouillard, T. Belytschko, Acta Mech. 213 (1–2) (2010) 53–69.
[4] L. Chen, T. Rabczuk, S.P.A. Bordas, G. Liu, K. Zeng, P. Kerfriden, Comput. Method. Appl. Mech. Eng. 209 (2012) 250–265.
[5] S. Bordas, S. Natarajan, P. Kerfriden, C.E. Augarde, D.R. Mahapatra, T. Rabczuk, S.D. Pont, Int. J. Numer. Meth. Eng. 86 (4–5) (2011) 637–666.
[6] I. Babuška, U. Banerjee, J.E. Osborn, Int. J. Comput. Meth. 1 (01) (2004) 67–103.
[7] N. Vu-Bac, H. Nguyen-Xuan, L. Chen, C.K. Lee, G. Zi, X. Zhuang, G.R. Liu, T. Rabczuk, J. Appl. Math. 2013 (2013).
[8] T. Belytschko, J. Lin, Comput. Struct. 25 (1987) 95–104.
[9] G.R. Johnson, R.A. Stryk, Int. J. Impact Eng. 5 (1) (1987) 411–421.
[10] R. Fan, J. Fish, Int. J. Numer. Meth. Eng. 73 (11) (2008) 1607.
[11] Y. Liu, V. Filonova, N. Hu, Z. Yuan, J. Fish, Z. Yuan, T. Belytschko, Int. J. Numer. Methods Eng. 99 (12) (2014) 867–887.
[12] J.H. Song, H. Wang, T. Belytschko, Comput. Mech. 42 (2) (2008) 239–250.
[13] X.P. Xu, A. Needleman, J. Mech. Phys. Solids 42 (9) (1994) 1397–1434.
[14] G.T. Camacho, M. Ortiz, Int. J. Solids Struct. 33 (20) (1996) 2899–2938.
[15] Y. Rashid, Nucl. Eng. Des. 7 (4) (1968) 334–344.
[16] Z.P. Baiant, L. Cedolin, J. Struct. Eng. 109 (1) (1983) 69–92.
[17] A. Karma, D.A. Kessler, H. Levine, Phys. Rev. Lett. 87 (4) (2001) 045501.
[18] H. Henry, H. Levine, Phys. Rev. Lett. 93 (10) (2004) 105504.
[19] G.A. Francfort, J.J. Marigo, J. Mech. Phys. Solids 46 (8) (1998) 1319–1342.
[20] B. Bourdin, G.A. Francfort, J.J. Marigo, J. Mech. Phys. Solids 48 (4) (2000) 797–826.
[21] C. Miehe, F. Welschinger, M. Hofacker, Int. J. Numer. Method. Eng. 83 (10) (2010) 1273–1311.
[22] C. Kuhn, R. Müller, Eng. Fract. Mech. 77 (18) (2010) 3625–3634.
[23] A. Schlüter, A. Willenbücher, C. Kuhn, R. Müller, Comput. Mech. 54 (5) (2014) 1141–1161.
[24] M.A. Msekh, J.M. Sargado, M. Jamshidian, P.M. Areias, T. Rabczuk, Comput. Mater. Sci. 96 (2015) 472–484.
[25] C. Miehe, M. Hofacker, F. Welschinger, Comput. Method. Appl. Mech. Eng. 199 (45) (2010) 2765–2778.
[26] M.J. Borden, C.V. Verhoosel, M.A. Scott, T.J. Hughes, C.M. Landis, Comput. Method. Appl. Mech. Eng. 217 (2012) 77–95.
[27] M. Hofacker, C. Miehe, Int. J. Numer. Meth. Eng. 93 (3) (2013) 276–301.
[28] M.J. Borden, T.J. Hughes, C.M. Landis, C.V. Verhoosel, Comput. Method. Appl. Mech. Eng. 273 (2014) 100–118.
[29] C.V. Verhoosel, R. Borst, Int. J. Numer. Meth. Eng. 96 (1) (2013) 43–62.
[30] C. Hesch, K. Weinberg, Int. J. Numer. Meth. Eng. 99 (12) (2014) 906–924.
[31] C. Miehe, M. Hofacker, L.M. Schänzel, F. Aldakheel, Comput. Method. Appl. Mech. Eng. 294 (2014) 486–522.
[32] H. Ulmer, M. Hofacker, C. Miehe, PAMM 13 (1) (2013) 533–536.
[33] M. Ambati, T. Gerasimov, L. De Lorenzis, Comput. Mech. (2015) 1–24.
[34] E. Giner, N. Sukumar, J. Tarancon, F. Fuenmayor, Eng. Fract. Mech. 76 (3) (2009) 347–368.
[35] J. Shi, D. Chopp, J. Lua, N. Sukumar, T. Belytschko, Eng. Fract. Mech. 77 (14) (2010) 2840–2863.
[36] B. Bourdin, Interf. Free Bound. 9 (3) (2007) 411–430.
[37] H. Amor, J.J. Marigo, C. Maurini, J. Mech. Phys. Solids 57 (8) (2009) 1209–1229.
[38] K. Pham, H. Amor, J.J. Marigo, C. Maurini, Int. J. Damage Mech. 20 (4) (2011) 618–652.
[39] C. Miehe, M. Lambrecht, Commun. Numer. Meth. Eng. 17 (5) (2001) 337–353.
[40] Abaqus, Abaqus Theory Manual and User's Manual, Dassault Systemes Simulia Corp., Providence, RI, USA, 2012.
[41] T. Belytschko, W.K. Liu, B. Moran, K. Elkhodary, Nonlinear Finite Elements for Continua and Structures, John Wiley & Sons, 2013.
[42] J. Ožbolt, J. Bošnjak, E. Sola, Int. J. Solids Struct. 50 (25) (2013) 4270–4278.
[43] J. Ožbolt, A. Sharma, H.W. Reinhardt, Int. J. Solids Struct. 48 (10) (2011) 1534–1543.
[44] A. Mesgarnejad, B. Bourdin, M. Khonsari, Comput. Method. Appl. Mech. Eng. 290 (2015) 420–437.